

# LYMAN- $\alpha$ TRANSIT SPECTROSCOPY AND THE NEUTRAL HYDROGEN TAIL OF THE HOT NEPTUNE GJ436B

JENNIFER R. KULOW<sup>1</sup>, KEVIN FRANCE<sup>1,3</sup>, JEFFERY LINSKY<sup>2</sup>, AND R. O. PARKE LOYD<sup>1</sup>

*Draft version March 8, 2021*

## ABSTRACT

To date, more than 750 planets have been discovered orbiting stars other than the Sun. Two subclasses of these exoplanets, “hot Jupiters” and their less massive counterparts “hot Neptunes,” provide a unique opportunity to study the extended atmospheres of planets outside of our solar system. We describe here the first far-ultraviolet transit study of a hot Neptune, specifically GJ436b, for which we use *HST*/STIS Lyman- $\alpha$  spectra to measure stellar flux as a function of time, observing variations due to absorption from the planetary atmosphere during transit. This analysis permits us to derive information about atmospheric extent, mass-loss rate from the planet, and interactions between the star and planet. We observe an evolution of the Lyman- $\alpha$  lightcurve with a transit depth of GJ436b from  $8.8 \pm 4.5\%$  near mid-transit, to  $22.9 \pm 3.9\% \sim 2$  hours after the nominal geometric egress of the planet. Using data from the time-tag mode and considering astrophysical noise from stellar variability, we calculate a post-egress occultation of  $23.7 \pm 4.5\%$ , demonstrating that the signature is statistically significant and of greater amplitude than can be attributed to stellar fluctuations alone. The extended egress absorption indicates the probable existence of a comet-like tail trailing the exoplanet. We calculate a mass-loss rate for GJ436b in the range of  $3.7 \times 10^6 - 1.1 \times 10^9 \text{ g s}^{-1}$ , corresponding to an atmospheric lifetime of  $4 \times 10^{11} - 2 \times 10^{14}$  years.

*Subject headings:* planets and satellites: atmospheres – planets and satellites: individual (GJ436b)

## 1. INTRODUCTION

Since the mid-1990’s, astronomers have been regularly discovering planets orbiting other stars using the radial velocity method (Mayor & Queloz 1995). Many of these planets called “hot Jupiters” are massive ( $\gtrsim 50 M_{\oplus} \gtrsim 0.15 M_{\text{Jup}}$ ), orbit very close to their host stars ( $\leq 0.05 \text{ AU}$ ), and have orbital periods of only a few days (Seager & Deming 2010). Less massive planets ( $10 - 50 M_{\oplus} \approx 0.03 - 0.15 M_{\text{Jup}} \approx 0.6 - 3 M_{\text{Nep}}$ ), that also orbit very close to their host stars, are similarly named after their solar system analogs, “hot Neptunes.” The majority of the first exoplanet detections were “hot Jupiters” and “hot Neptunes” because there is a detection bias in favor of this type of planet. Since they are large (in mass and radius) and orbit close to their host stars, they are more easily detected in both radial velocity and transit searches.

In 1999, Henry et al. (2000) discovered the first transiting exoplanet, HD209458b. Transiting exoplanets provide an opportunity to study the composition and structure of their atmospheres, because as these planets pass in front of their host star, their atmosphere blocks a portion of the starlight. Spectroscopy at IR and optical wavelengths has led to the discovery of Na I, H<sub>2</sub>O, CH<sub>4</sub>, and CO (Charbonneau et al. 2002; Tinetti et al. 2007; Swain et al. 2008; Swain et al. 2009) in the atmospheres of exoplanets, shifting the emphasis of exoplanet studies toward detecting and characterizing their atmospheres

(Koskinen et al. 2010).

While many studies utilize IR (700 nm – 3  $\mu\text{m}$ ) (e.g. Deming et al. 2007) and optical (400 – 700 nm) (e.g. Butler et al. 2004) wavelengths, UV (1000 – 4000  $\text{\AA}$ ) observations provide a unique opportunity to characterize exoplanet exospheres. Stellar FUV and EUV radiation heats, accelerates, and, when the photon energies exceed 13.6 eV, ionizes the hydrogen in the upper atmosphere (Murray-Clay et al. 2009). When the thermal energy exceeds the gravitational potential energy ( $3kT/2 > GMm/r$ ), the heated gas expands (Lammer et al. 2003) and likely escapes from the planet. These inflated atmospheres contain many atomic species, such as H, C<sup>+</sup>, O, and Si<sup>2+</sup>, that absorb the stellar radiation in UV resonance lines (Vidal-Madjar et al. 2004; Linsky et al. 2010). Because the envelopes of these exoplanets are inflated, the geometric area in their UV resonance lines is larger than that of molecules detected in the IR and optical, and the transit depth will be larger. Such data permit us to understand the composition of extended exoplanet atmospheres.

Vidal-Madjar et al. (2003) used the H I Lyman- $\alpha$  1215  $\text{\AA}$  emission line of HD209458 to obtain the first evidence of an inflated exoplanetary atmosphere, revealing a transit depth in Lyman- $\alpha$  ( $15 \pm 4\%$ ) several times that of the geometric depth determined from the optical transit ( $1.58 \pm 0.18\%$ ). The Lyman- $\alpha$  transit depth indicates an atmosphere that extends beyond its Roche lobe, likely indicating atmospheric escape. Subsequent UV observations have demonstrated the existence of enlarged envelopes in the spectral lines of O, C<sup>+</sup> (Vidal-Madjar et al. 2004), and Si<sup>2+</sup> (Linsky et al. 2010) around HD209458b, and later observations identified a similar absorption spectrum from the atmosphere of HD189733b. Observations of HD189733 have been

<sup>1</sup>Center for Astrophysics and Space Astronomy, University of Colorado, 593 UCB Boulder, CO 80309-0593, USA; jennifer.kulow@colorado.edu, kevin.france@colorado.edu, robert.loyd@colorado.edu

<sup>2</sup>JILA, University of Colorado and NIST, 440 UCB Boulder, CO 80309-0440, USA; jlinsky@jilau1.colorado.edu

<sup>3</sup>NASA Nancy Grace Roman Fellow

used to detect extended atmospheres in lines of H I (Lecavelier des Etangs et al. 2010), O I, and possibly C II (Ben-Jaffel & Ballester 2013). The non-detection of an extended Lyman- $\alpha$  envelope in April 2010, indicated significant variations in the evaporation rate of H I (Lecavelier des Etangs et al. 2012).

UV transit observations are often used to infer mass-loss rates of hot Jupiters, from which we may learn about the evolution of exoplanets and their atmospheres. Vidal-Madjar et al. (2003) used a particle simulation to limit the mass loss rate of HD209458b to  $\geq 10^{10}$  g s $^{-1}$ . Linsky et al. (2010) performed a theoretical calculation to find mass-loss rates in the range of  $(8 - 40) \times 10^{10}$  g s $^{-1}$ . Lecavelier des Etangs et al. (2010) used their data of HD189733b and a numerical simulation to find a best fit mass-loss rate of  $10^{10}$  g s $^{-1}$ . Ehrenreich & Désert (2011) compare the planet gravitational potential energy to the stellar X/EUV energy deposited in the atmosphere and estimate the mass-loss rate for WASP-12b to be  $2.5 \times 10^{11}$  g s $^{-1}$ .

Many theoretical models have been developed to explain the evaporation process and to predict the mass-loss rates for various hot Jupiters. Lammer et al. (2003) used the heating rate from stellar X-ray and EUV radiation to estimate a mass-loss rate for HD209458b of  $\sim 10^{12}$  g s $^{-1}$ . Yelle (2004) (later revised in Yelle 2006) included chemical calculations to estimate a mass-loss rate. Cooling from H $_3^+$  and ionization of H to H $^+$ , reducing the amount of stellar energy available for heating, led to a lower mass-loss rate of  $4.7 \times 10^{10}$  g s $^{-1}$ . Similar calculations by García Muñoz (2007) determined mass-loss rates in the range  $6 - 15 \times 10^{10}$  g s $^{-1}$  depending on the level of stellar activity. Holmström et al. (2008) attributed a portion of the Lyman- $\alpha$  absorption to protons from the stellar wind that have been neutralized by charge exchange with hydrogen atoms in the planetary atmosphere and calculated a mass-loss rate of  $7 \times 10^8$  g s $^{-1}$ . Guo (2013) calculated a mass-loss rate of  $4.3 \times 10^9$  g s $^{-1}$  using a two-dimensional model that assumed HD209458b is tidally locked with one side of the planet always facing the star. Murray-Clay et al. (2009) modeled the atmospheric escape of a theoretical hot Jupiter (similar to HD209458b) that includes realistic heating and cooling rates, ionization balance, tidal gravity, and pressure confinement by the stellar wind. They found a mass-loss rate of  $2 \times 10^{10}$  g s $^{-1}$ . In the above examples, the calculated mass-loss rates vary by several orders of magnitude depending on what physics is considered and on the values of system parameters (for example the amount of stellar EUV flux).

The manner in which the atmospheric envelope interacts with the stellar wind determines the structure of the gas around the planet. High-velocity neutral hydrogen escaping from the atmosphere trails the planet absorbing Lyman- $\alpha$  photons until the hydrogen is ionized by the stellar EUV flux or charge exchanges with stellar wind protons. The trailing material may cause the hydrogen Lyman- $\alpha$  transit to last longer than the optical occultation. The formation of a comet-like tail trailing the planet was first suggested by Schneider et al. (1998). Models of neutral hydrogen escaping from the hot Jupiter HD209458b and HD189733b by Bourrier & Lecavelier des Etangs (2013)

support this structure. The evaporating super-Mercury exoplanet KIC 12557548b likely has a dusty comet-like tail (Rappaport et al. 2012; Budaj 2013) and the extreme hot Jupiter WASP-12b is losing sufficient mass to completely obscure its host star's emission in the cases of the Mg II h and k lines (Haswell et al. 2012).

Vidal-Madjar et al. (2003) observed absorption out to Doppler velocities  $\pm 100$  km s $^{-1}$  from the Lyman- $\alpha$  line center of HD209458b, and absorption has been seen at velocities as large as  $-230$  km s $^{-1}$  from the center of Lyman- $\alpha$  for HD189733b (Lecavelier des Etangs et al. 2012). Thermal velocities can only account for absorption out to  $\sim 10$  km s $^{-1}$  (Murray-Clay et al. 2009). Models by Lecavelier des Etangs et al. (2012) suggest that stellar radiation pressure can accelerate particles up to  $120$  km s $^{-1}$ , but an additional mechanism is necessary to explain the large observed radial velocities. Charge exchange with hot, slow ( $< 50 - 100$  km s $^{-1}$ ) stellar wind protons can produce the observed velocities (Holmström et al. 2008; Ekenbäck et al. 2010; Tremblin & Chiang 2013). Holmström et al. (2008) proposed that the absorption in neutral hydrogen at high velocities is due to charge exchange between protons from the stellar wind and planetary neutral hydrogen. The planetary hydrogen is ionized and the stellar wind proton becomes neutral hydrogen maintaining its large velocity.

### 1.1. Previous Studies of GJ436b

A promising exoplanet for UV transit observations is GJ436b, a hot Neptune, ( $M = 0.07 M_{\text{Jup}}$ ), orbiting an M2 dwarf at 0.029 AU with a period of 2.6 days. GJ436b is particularly promising because it is very close to Earth, at a distance of only 10.2 pc. The properties of the system are summarized in Table 1. GJ436b was discovered by Butler et al. (2004) using the radial velocity method, but was later found to be transiting its host star (Gillon et al. 2007).

In 2010 *Spitzer* observed GJ436 during several secondary transits in 6 bands from  $3.6 - 24$   $\mu\text{m}$ . Using a Metropolis-Hastings Markov-chain Monte Carlo (MCMC) model, Stevenson et al. (2010) explored a wide range of parameter space to determine the best-fit compositional models. They found a high CO abundance and a deficiency of CH $_4$  relative to thermochemical equilibrium. Madhusudhan & Seager (2011) also used MCMC to confirm the overabundance of CO and CO $_2$ , and a slight underabundance of H $_2$ O, as compared to equilibrium chemistry with solar metallicity. They explained the observed abundances by a combination of high metallicity ( $\sim 10\times$  solar) and vertical mixing. Observations by Knutson et al. (2014) indicate an effectively featureless transmission spectrum, ruling out cloud-free, hydrogen-dominated atmosphere models. The measured spectrum is consistent with either a high cloud or haze layer or with a relatively hydrogen-poor atmospheric composition. Hu & Seager (2014) find that hot Neptunes, like GJ436b, are likely to have thick atmospheres that are not hydrogen dominated, but are water-rich or hydrocarbon-rich depending on their C/O ratio. Using limited *HST*/STIS data of the stellar Lyman- $\alpha$  flux, Ehrenreich et al. (2011) developed numerical simulations to determine the transit signature of GJ436b for various assumed mass-loss rates. They predicted an 11% transit

depth in Lyman- $\alpha$  for a mass-loss rate of  $10^{10}$  g s $^{-1}$ . The analysis we have conducted is the first to place observational constraints on the mass-loss rate of GJ436b or any other Neptune-mass exoplanet.

In this paper, we present and analyze transit observations of GJ436b in Lyman- $\alpha$  observed with Space Telescope Imaging Spectrograph (STIS) on the *Hubble Space Telescope* (*HST*). In Section 2 we describe the data sets used and the reduction process, and how we created the lightcurves and velocity profiles. We present the lightcurve and velocity profile for Lyman- $\alpha$  in Section 3 along with the measured absorption depths. In Section 4 we discuss the structure of the system and calculate a range of mass-loss rates for GJ436b. We summarize our results in Section 5.

## 2. OBSERVATIONS AND DATA ANALYSIS

### 2.1. GJ436 Data

The *HST*/STIS transit data of GJ436 were obtained with the G140M grating using a long slit with dimensions  $52'' \times 0.1''$ . We selected a central wavelength of 1222 Å, covering the spectral range of 1194 Å - 1249 Å with a spectral resolution of about 25 km s $^{-1}$ . The data were taken with the FUV-MAMA detector using the time-tag mode. Table 2 summarizes all of the observations. Our four orbit per transit observing cadence is comparable to that used by Lecavelier des Etangs et al. (2012) for velocity resolved observations of the extended hydrogen atmosphere of the hot Jupiter HD 189733b with the same STIS grating configuration. Given an error of 2%, the relative photometric accuracy of STIS, issues of persistence and instrumental settling are less significant when observing the 10% UV transit signal of the exosphere compared to the < 1% near-IR molecular diagnostics of the lower atmosphere.

We reduced the GJ436 data using CALSTIS v2.40 (2012 May 23). For the final two exposures, the CALSTIS pipeline did not correctly extract the one-dimensional spectrum (the “x1d” file) from the two-dimensional data. We therefore manually extracted the one-dimensional spectrum for all four exposures. Since in the “x2d” file, the source was located at pixels 481 – 491, we subtracted a background ribbon at pixels 492 – 502 from the source data (see Figure 1). A wavelength solution was then calculated by using the reference wavelength, reference pixel, and dispersion from the header. Finally, we obtained fluxes by multiplying by the angular area covered by the pixels and an additional scale factor (determined empirically by matching to a correctly extracted spectrum from the “x1d” files for the first two exposures).

### 2.2. Data Analysis

To characterize the transit, we take two complementary approaches. The first is the creation and analysis of lightcurves. This approach allows us to study the transit with higher time resolution. The lightcurve creation method is described in detail below. In the second method, we analyze the spectral difference between the pre-ingress, transit, and post-egress data. This method maintains the velocity resolution of the data. We also created velocity profiles for Lyman- $\alpha$ . We compared the pre-ingress spectrum to the transit and post-egress spec-

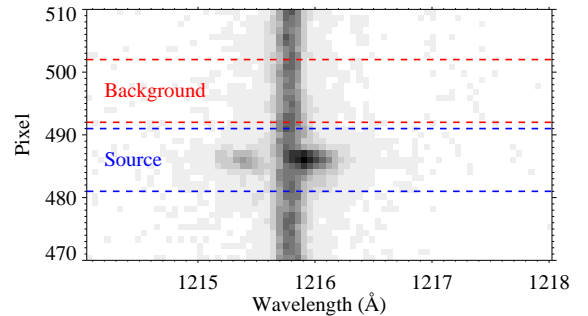


FIG. 1.— 2-D STIS data of GJ436. The source ribbon used to extract the 1-D spectrum is marked in blue. The ribbon used for background subtraction is shown in red. The vertical stripe in the image is geocoronal Lyman- $\alpha$  restricted by the STIS slit.

tra as a function of velocity. We also looked at the difference between the spectra (pre-ingress minus post-egress, such that absorption is a positive difference) vs. velocity. We then calculated the post-egress depth by integrating this difference spectrum.

#### 2.2.1. Light Curve Creation

The data were obtained over a time period that covers portions of the exoplanet orbit before, during, and after transit. For every exposure, we calculated the orbital phase of the exoplanet (in hours) at the time of mid-exposure using the ephemeris data in Table 1, such that mid-transit occurs at phase 0 hours.

We used the 1-D spectra extracted from the “x2d” files, as described in Section 2.1, and integrated the flux for different wavelength portions of the Lyman- $\alpha$  line. Avoiding the center of the Lyman- $\alpha$  line, where noise from the airglow subtraction is high, we integrated the flux from the blue and red sides of the line separately. The wavelength range for the integration of each wing of Lyman- $\alpha$  is shown in Table 3. We then created lightcurves for each wing by plotting the total flux vs. orbital phase.

We also used the “tag” files containing the time-tag data to calculate a time series of the data in 12 minute increments. The “tag” files contain a photon event list giving the time and detector coordinates of each recorded count. Using the known positions of the source and the background as well as the wavelength solution (from the “x2d” files), we keep only events with detector positions that correspond to source or background counts within specified wavelength ranges. These data are then binned in time. We found that a bin size of 12 minutes is a suitable compromise between signal-to-noise and time resolution. This additional time resolution allows us to better assess the lightcurve for stellar variability (Lloyd & France 2014). We incorporated these time-tag data in the Lyman- $\alpha$  lightcurve analysis for GJ436.

## 3. RESULTS AND DISCUSSION

### 3.1. GJ436b Transit

We show the Lyman- $\alpha$  lightcurve for GJ436 in Figure 2 and the Lyman- $\alpha$  velocity profile in Figure 3. Table 4 shows the transit depths extracted from these figures. The transit depths are identical for the two procedures (because the reference spectrum and the integration method are the same), however, the spectral analysis results in somewhat larger errors, due to the extra step of subtracting prior to normalizing and integrating. We will use the higher time resolution lightcurve

TABLE 1  
 PROPERTIES OF GJ436 AND GJ436B

Property	Value	Reference
Host Star Spectral Type	M2 V	Butler et al. (2004)
Distance (pc)	$10.14^{+0.25}_{-0.23}$	van Leeuwen (2007)
$M_*/M_\odot$	$0.452^{+0.014}_{-0.012}$	Torres et al. (2008)
$R_*/R_\odot$	$0.464^{+0.009}_{-0.011}$	Torres et al. (2008)
$P_{orbit}$ (days)	$2.643850 \pm 9 \times 10^{-5}$	Pont et al. (2009)
Transit Center (JD)	$2454279.436714 \pm 1.5 \times 10^{-5}$	Pont et al. (2009)
RA (h:m:s)	+11:42:11.18	Zacharias et al. (2012)
Dec (d:m:s)	+26:42:22.64	Zacharias et al. (2012)
$R_{planet}/R_{Jup}$	$0.3767^{+0.0082}_{-0.0092}$	Torres et al. (2008)
$M_{planet}/M_{Jup}$	$0.0727 \pm 0.0032$	Butler et al. (2006)
Semimajor axis (AU)	$0.02872 \pm 0.0048$	Butler et al. (2006)
Transit duration (hours)	$0.7608 \pm 0.012$	Pont et al. (2009)
Transit depth for $R_{planet}$	$0.00696 \pm 0.000117$	Torres et al. (2008)
Escape speed from GJ436b ( $\text{km s}^{-1}$ )	26.4	
Orbital velocity amplitude ( $\text{km s}^{-1}$ )	118	
Radial Velocity ( $\text{km s}^{-1}$ )	$9.6 \pm 0.1$	Nidever et al. (2002)

 TABLE 2  
 SUMMARY OF OBSERVATIONS

Data Set	Exp. Time (s)	Day	Start (UT)	Phase (hr) <sup>a,b</sup>
obgh0710	1515.145	Dec 7, 2012	9:48:48	-01:02:17.1
obgh0720	2905.121	Dec 7, 2012	10:58:55	00:21:25.3
obgh0730	2905.193	Dec 7, 2012	12:34:38	01:57:08.8
obgh0740	2905.172	Dec 7, 2012	14:10:21	03:32:52.4

<sup>a</sup> Phases shown are at the time of mid-exposure.

<sup>b</sup> A phase of 0:00:00 corresponds to the center of the primary optical transit.

 TABLE 3  
 LYMAN- $\alpha$  WINGS

	Wavelengths Integrated ( $\text{\AA}$ )	Velocities Integrated ( $\text{km s}^{-1}$ )
Blue Wing	1214.8 – 1215.6	-214.6 – -17.3
Red Wing	1215.9 – 1216.5	56.7 – 204.7

data to analyze the transit depth. For GJ436b we see a mid-transit depth of  $16.6 \pm 7.2\%$  in the blue wing and  $4.5 \pm 5.7\%$  in the red wing. This corresponds to an occulting disk of  $5.0 R_p$  and  $2.6 R_p$  respectively, both smaller than the Roche lobe radius of  $6.1 R_p$ . When both wings are combined, the mid-transit depth is  $8.8 \pm 4.5\%$ , corresponding to an equivalent opaque occulting disk of  $3.6 R_p$ . The asymmetry in the absorption can be explained by charge exchange of the stellar wind with the atmosphere. As viewed from Earth, only the stellar wind traveling towards us can be observed, causing excess absorption blue-ward of line center. This type of asymmetry, with more absorption in the blue wing, is also seen in the Lyman- $\alpha$  absorption during transit from HD209458b (Vidal-Madjar et al. 2003) and HD189733b (Lecavelier des Etangs et al. 2012).

Interestingly, the Lyman- $\alpha$  transit extends much later in phase than the optical transit. We examine these data for the possibility of extended egress, finding post-egress depths of  $29.9 \pm 6.4\%$  in the blue wing,  $19.1 \pm 5.0\%$  in the red wing, and  $22.9 \pm 3.9\%$  for both wings combined  $\sim 2$  hours after mid-transit and about 1.5 hours after fourth contact. The time-tag data points are presented in Ta-

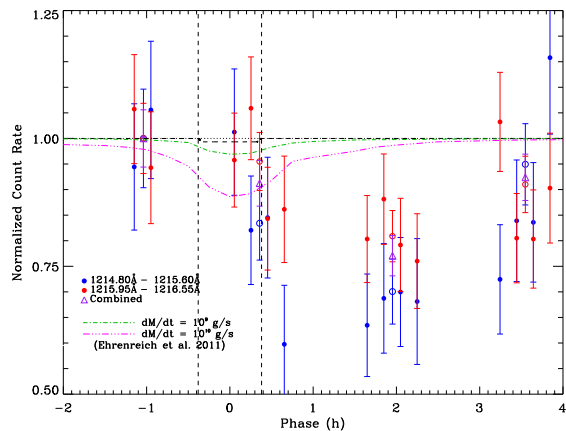


FIG. 2.— Normalized Lyman- $\alpha$  count rates for GJ436. Blue points show the flux from the blue wing of Lyman- $\alpha$  and red points show the flux from the red wing. Filled points are calculated from the time-tag data, while the open circles are from the entire exposure. Error bars indicate  $\pm 1\sigma$ . The black dotted line indicates the normalized flux level, while the black dashed line shows the transit curve as calculated from the optical transit parameters. The green and pink lines show the predicted transit signature of GJ436b as calculated by Ehrenreich et al. (2011) for mass-loss rates of  $10^9$  and  $10^{10} \text{ g s}^{-1}$  respectively. Vertical dashed lines indicate first and fourth contacts.

 TABLE 4  
 TRANSIT DEPTHS FOR GJ436 FULL EXPOSURES

Species	Transit Depth from Difference Spectrum	Transit Depth from Lightcurve
Lyman- $\alpha$ Blue Wing mid-transit	$16.6 \pm 8.2\%$	$16.6 \pm 7.2\%$
Lyman- $\alpha$ Red Wing mid-transit	$4.5 \pm 5.9\%$	$4.5 \pm 5.7\%$
Lyman- $\alpha$ coadded mid-transit	$8.8 \pm 4.8\%$	$8.8 \pm 4.5\%$
Lyman- $\alpha$ Blue Wing post-egress	$29.9 \pm 8.3\%$	$29.9 \pm 6.4\%$
Lyman- $\alpha$ Red Wing post-egress	$19.1 \pm 5.8\%$	$19.1 \pm 5.0\%$
Lyman- $\alpha$ coadded post-egress	$22.9 \pm 4.8\%$	$22.9 \pm 3.9\%$

ble 5. These data corroborate the detection of both the transit and extended egress, as three of the four transit data points and all of the post-egress data points show a transit detection, although large variations in the blue-wing time-tag data are observed near mid-transit.

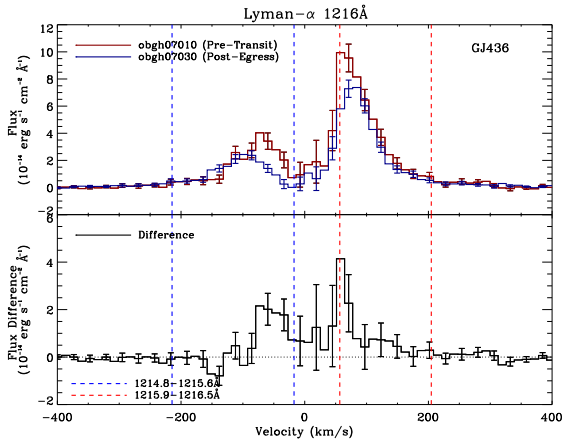


FIG. 3.— Lyman- $\alpha$  velocity profile for GJ436. The top panel compares the pre-ingress spectrum, in dark red, to the post-egress spectrum, in dark blue, and the bottom panel shows the difference between these spectra, pre-ingress minus post-egress. Error bars indicate  $\pm 1\sigma$ . The regions of integrated flux are also shown; the blue wing is between the blue dashed lines and the red wing is between the red dashed lines. During the post-egress time interval, we find an occultation depth of  $29.9 \pm 8.3\%$  in the Lyman- $\alpha$  blue wing,  $19.1 \pm 5.8\%$  in the Lyman- $\alpha$  red wing, and  $22.9 \pm 4.8\%$  in the combined wings of the Lyman- $\alpha$  line.

TABLE 5  
TRANSIT DEPTHS FOR GJ436 TIME-TAG POINTS

Phase (hr)	Transit Depth in Blue Wing	Transit Depth in Red Wing
-1:08:54.7	$5.6 \pm 12.3\%$	$-5.7 \pm 10.7\%$
-0:56:54.7	$-5.6 \pm 13.4\%$	$5.7 \pm 10.9\%$
0:03:12.3	$-1.2 \pm 12.4\%$	$4.2 \pm 9.2\%$
0:15:12.3	$18.0 \pm 10.6\%$	$-5.9 \pm 10.0\%$
0:27:12.3	$15.5 \pm 11.8\%$	$15.7 \pm 10.1\%$
0:39:12.3	$40.2 \pm 11.5\%$	$13.9 \pm 10.4\%$
1:38:55.3	$36.5 \pm 10.0\%$	$19.7 \pm 8.5\%$
1:50:55.3	$31.3 \pm 10.7\%$	$11.9 \pm 8.8\%$
2:02:55.3	$30.0 \pm 10.7\%$	$20.8 \pm 9.1\%$
2:14:38.5	$31.9 \pm 12.3\%$	$24.0 \pm 9.3\%$
3:14:38.4	$27.6 \pm 10.7\%$	$-3.2 \pm 9.7\%$
3:26:38.4	$16.1 \pm 11.9\%$	$19.5 \pm 8.7\%$
3:38:38.4	$16.4 \pm 11.7\%$	$19.7 \pm 9.6\%$
3:50:38.4	$-15.8 \pm 15.0\%$	$9.7 \pm 10.7\%$

### 3.2. Extended Egress in GJ436

To determine whether or not the extended egress is real, we consider the time-tag data. We form the null hypothesis that the data are Gaussian distributed and the apparent occultation is random noise. We use the average of the error bars on the time-tag data as the standard deviation for the Gaussian distributions ( $\sigma_{blue} = 0.1092, \sigma_{red} = 0.08930$ ), both with a mean of unity. Assuming these distributions, we determined the probability of finding four consecutive points lower than the highest point in the set of four at the deepest transit depth, which is located at phase  $\sim 2$  hours ( $x_{blue} = 0.3003, x_{red} = 0.1187$  below the mean). We did this by randomly picking 14 points from the specified Gaussian distribution and counting how many trials out of  $10^7$  had four consecutive points outside the requisite range. For the parameters determined for the blue wing, none of the  $10^7$  trials had four consecutive points. For the red wing distribution, we found a probability of  $9.31 \pm 0.76 \times 10^{-5}$  to randomly produce the result. We

therefore conclude that the deep, extended egress signal seen in Figure 2 is real and not due to random statistical variations.

### 3.3. Stellar Variability of GJ436

While we have determined that the post-egress detection is not due to statistical noise, we have not yet considered whether the drop in flux could be due to stellar variability, as opposed to atmospheric absorption from GJ436b. To address this issue, we look at a resonance line from N V, an ion that we do not expect to find in the atmosphere of the exoplanet. For the N V time-tag data points we find  $RMS = 0.2765$ , while the average value of the  $1\sigma$  error bar for those points is 0.4010. We conclude that the signal to noise is too low for the N V doublet to be a suitable tracer of stellar variability. Similarly, there was not enough flux in the Si III line to be measurable above the noise.

Instead we look to the literature to assess the potential magnitude of stellar variability. Loyd & France (2014) studied time variability in the C II, Si III, and Si IV resonance lines of 38 cool stars, including GJ436. They did not attempt to characterize Lyman- $\alpha$  line variability because geocoronal airglow cannot be removed reliably from their COS data. Instead we use their C II emission line variability, because C II has a similar formation temperature to Lyman- $\alpha$  ( $T_{form} \approx (1-3) \times 10^4$  K, Dere et al. 2009). Loyd & France (2014) found that the mean-normalized chromospheric C II line variability, excluding flare periods, in GJ436 is  $0.20_{0.12}^{0.99}$  on 60 second timescales. Our post-egress data cover a 48 minute time span. Assuming that the stellar variability is uncorrelated over time, the noise associated with stellar fluctuations is estimated to be  $0.20/\sqrt{48} = 0.0289$ . Combining the 8 post-egress time-tag data points and the photon noise with the upper limit on the noise expected from chromospheric variability, we find a 23.7% occultation with an uncertainty of 4.5%. From this we conclude that the post-egress detection is very likely real. Future observations over several transit cycles would be very valuable.

## 4. GJ436 SYSTEM

### 4.1. Structure

Some models of the interaction between escaping gas from the exoplanet's atmosphere and the stellar wind predict a comet-like tail extending behind the planet (Schneider et al. 1998; Bourrier & Lecavelier des Etangs 2013). The Lyman- $\alpha$  data support this type of structure in the GJ436 system. A large, inflated cloud of gas trailing the planet could explain an occultation deeper than that observed in the optical and post-egress absorption long after optical transit.

In order to simulate the structure of the exoplanetary gas cloud at the orbit of GJ436b, we attenuate the pre-ingress profile by a column of hydrogen and deuterium to match the post-egress spectrum. We search for a  $\chi^2$  best fit neutral hydrogen column ( $[\log(N_{HI})]$  ranging from 14.0 to 19.0 in step sizes of 0.2 dex) for a grid of stellar covering fraction (assuming uniform optical thickness of the gas over the area covered and uniform emission of Lyman- $\alpha$  from the stellar disk) vs. Doppler  $b$ -value,  $b = (\frac{2kT}{m_H} + v_{turb}^2)^{1/2}$ . We assume a fixed D/H ratio of  $1.5 \times 10^{-5}$  (Linsky et al. 2006). For the range

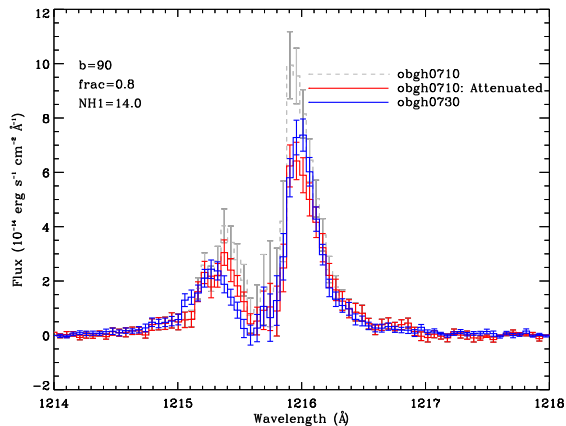


FIG. 4.— Lyman- $\alpha$  profile attenuation. The gray curve shows the Lyman- $\alpha$  profile pre-egress, and the blue curve shows the profile observed post-egress. The red curve shows the pre-egress profile attenuated by a cloud of hydrogen and deuterium gas with a Doppler  $b$ -value of  $90 \text{ km s}^{-1}$ , a covering fraction 0.8, and a  $\chi^2$  best fit column density of  $N_{\text{H}} = 10^{14.0} \text{ cm}^{-2}$ . Error bars indicate  $\pm 1\sigma$ .

of tested covering fractions and  $b$ -values, we find two parameter regimes that provide a reasonable fit to the data. The first is a low covering fraction, high  $N_{\text{HI}}$  model. The second is a high covering fraction low  $N_{\text{HI}}$  model. We expect the second regime to be more physically plausible. The low covering fraction models require  $N_{\text{HI}} \sim 10^{19} \text{ cm}^{-2}$ . Assuming that the comet-like tail extends to a few times the orbital radius,  $\sim 0.1 \text{ AU}$  in the line of sight to the star, we find a number density  $n_{\text{H}} \sim \text{few} \times 10^7 \text{ cm}^{-3}$ . This density is far above the estimates ( $\sim 3 \times 10^5 \text{ cm}^{-3}$ ) from comet-like tail models (Bourrier & Lecavelier des Etangs 2013). A column density of  $N_{\text{HI}} = 10^{15} \text{ cm}^{-2}$ , typical of the high covering fraction regime, converts to a number density  $n_{\text{HI}} \sim \text{few} \times 10^4 \text{ cm}^{-3}$ .

Taking the high covering fraction and low  $N_{\text{HI}}$  case as more plausible, acceptable fits to the post-egress Lyman- $\alpha$  spectrum require the Doppler  $b$ -parameter to be between 60 and  $120 \text{ km s}^{-1}$ . We require  $b$ -values in this range to fit the shape of the post-egress Lyman- $\alpha$  profile. For a typical atmospheric temperature of  $10^4 \text{ K}$ , the thermal width is  $13 \text{ km s}^{-1}$ , requiring a superthermal velocity component of  $\sim 50$  to  $110 \text{ km s}^{-1}$  to explain such high  $b$ -values. Charge exchange between stellar wind protons and planetary wind neutral H atoms will lead to neutral H atoms with high velocities. For a representative covering fraction of 0.8, we can then limit  $\log(N_{\text{HI}})$  to 14 – 16. Figure 4 shows an example best fit attenuation profile with parameters within this range. These ranges are shown in Table 6.

To achieve a covering fraction of 0.8 requires a cloud of  $R \approx 10 R_{\text{planet}}$ . Using the column density and  $b$  (to calculate the cross-section at the line core,  $\sigma = \frac{\sqrt{\pi}e^2 f \Delta\lambda_0}{m_e c b}$ ), we can estimate the line center optical depth of the extended neutral hydrogen atmosphere ( $\tau_0 = N_{\text{H}}\sigma$ ). For the ranges of  $N_{\text{H}}$  and  $b$ , we find  $\tau_0 = 0.63 - 130$ . Koskinen et al. (2010) predict the hydrogen cloud to be optically thick in the line wings, indicating that our models with the lowest columns and higher  $b$ s (which give the higher  $\tau_{\nu}$ s) are more physically representative.

#### 4.2. GJ436b Mass-Loss Rate

TABLE 6  
CLOUD PROPERTIES

	Range
Covering fraction	0.7 – 0.9
$b$ ( $\text{km s}^{-1}$ )	60 – 120
$\log(N_{\text{HI}} [\text{cm}^{-2}])$	14 – 16
$\tau_0$	0.63 – 130

##### 4.2.1. Spherical Mass-Loss

We first calculate the mass-loss rate for GJ436b by assuming a spherically symmetric envelope around the planet that blocks a portion of the stellar surface. We consider a line of sight (LOS) toward the center of the star that passes through the exoplanet’s atmosphere a distance  $p$  from the center of the planet. We measure  $x$  along the LOS and  $r$  along from the center of the planet (see Figure 5). For a spherical outflow with a constant mass-loss rate, the mass flux in neutral hydrogen from the planet is

$$\dot{M}_{\text{HI}} = 4\pi r^2 m_{\text{H}} v n_{\text{HI}}(r), \quad (1)$$

where  $v$  is the outflow velocity at  $r$ . The optical depth at the line center along this LOS is

$$\tau_0 = \sigma \int_0^\infty n_{\text{HI}}(x) dx, \quad (2)$$

where  $n_{\text{HI}}$  is the number density of neutral hydrogen,  $\sigma$  is the absorption cross section. Combining Equations 1 and 2 yields

$$\tau_0 = \frac{\sigma \dot{M}_{\text{HI}}}{4\pi m_{\text{H}}} \int_0^\infty \frac{dx}{v r^2} \Rightarrow \dot{M}_{\text{HI}} = \frac{4\pi m_{\text{H}} \tau_0}{\sigma} \left[ \int_0^\infty \frac{dx}{v r^2} \right]^{-1} \quad (3)$$

In the integrand, the  $r^{-2}$  factor gives the highest weight to  $v$  values where the LOS passes closest to the planet (smallest  $r$ ). Thus, for an order-of-magnitude calculation  $v$  may be taken out of the integral and replaced with a value representative of that expected near the radius at closest approach,  $r = p$ , between the LOS and planet. (This assumes  $v$  does not drop precipitously at large  $r$ , consistent with the models of Murray-Clay et al. (2009).) Bringing  $v$  out of the integral, we are able to find an analytical solution. From Figure 5 we can use  $r^2 = (x - a)^2 + p^2$ , where  $a$  is the star-planet distance, to evaluate the integral in Equation 3.

$$\int_0^\infty \frac{dx}{r^2} = \int_0^\infty \frac{dx}{(x - a)^2 + p^2} = \frac{\pi}{2p} + \frac{1}{p} \arctan\left(\frac{a}{p}\right). \quad (4)$$

Since only LOSs that intersect the stellar disk,  $p < R_\star$ , are of interest, and for GJ436  $a/R_\star = 13.34$ ,  $\arctan(a/p)$  may be taken to be  $\pi/2$  to good accuracy, so that the integral in Equation 4 simplifies to  $\pi/p$ . Thus

$$\dot{M}_{\text{HI}} \approx \frac{4p v m_{\text{H}} \tau_0}{\sigma} \quad (5)$$

The cross section at line center is given by

$$\sigma_0 = \frac{\sqrt{\pi} e^2}{m_e c \Delta\nu_D} f \quad (6)$$

$f = 0.4161$  is the oscillator strength,  $m_e$  is the electron mass, and  $\Delta\nu_D$  is the Doppler width given by

$$\Delta\nu_D = \frac{\nu_0}{c} \left( \frac{2kT}{m_H} + v_{turb}^2 \right)^{1/2} = \frac{b}{\lambda_0}.$$

Given the range of  $b$ -values determined in Section 4.1 ( $b = 60 - 120 \text{ km s}^{-1}$ ), we limit the cross section at Lyman- $\alpha$  to  $\sigma_0(\text{HI}) = 6.3 \times 10^{-15} - 1.3 \times 10^{-14}$ .

Assuming the absorption is due to an optically thin cloud covering the star, we consider annuli of area  $2\pi p dp$  centered on the planet. Each annulus absorbs a fraction of the light from the stellar disk equal to

$$\frac{dF_\star}{F_\star} = \frac{2\pi p dp (1 - e^{-\tau_0})}{\pi R_\star^2} = \frac{2}{R_\star^2} p (1 - e^{-\tau_0}) dp, \quad (7)$$

where  $\tau_0 = \tau_0(p)$  is the optical depth at line center along the LOS passing through the annulus of radius  $p$ . The observed transit depth ( $\delta$ ) is then

$$\delta = \int_{R_p}^{R_\star} \frac{dF}{F} = \frac{2}{R_\star^2} \int_{R_p}^{R_\star} p (1 - e^{-\tau_0}) dp. \quad (8)$$

According to Murray-Clay et al. (2009),  $\tau_0 < 0.1$  for  $p \gtrsim 1.5R_p$ , so using the small  $\tau$  approximation, Equation 8 becomes

$$\delta = \frac{2}{R_\star^2} \int_{R_p}^{R_\star} p \tau_0 dp. \quad (9)$$

Using Equation 5 this becomes

$$\delta \approx \frac{2}{R_\star^2} \frac{\dot{M} \sigma_0}{4m} \int_{R_p}^{R_\star} \frac{dp}{v} \approx \frac{2}{R_\star^2} \frac{\dot{M} \sigma_0}{4mv} (R_\star - R_p) \approx \frac{2}{R_\star} \frac{\dot{M} \sigma_0}{4mv}. \quad (10)$$

While Murray-Clay et al. (2009) predict  $v$  to vary by a factor of a few over the range of  $p$  considered here, we have approximated  $v$  to be constant with  $p$ . We have also neglected the  $R_p \ll R_\star$  term. Solving for the mass loss rate, we get

$$\dot{M} \approx \frac{2\delta R_\star m v}{\sigma_0} \quad (11)$$

Following Murray-Clay et al. (2009), we adopt  $v = 10 \text{ km s}^{-1}$ , approximately equal to the thermal velocity of hydrogen at  $10^4 \text{ K}$ . We use the observed mid-transit depth  $\delta = 0.088 \pm 0.045$ . Thus, these observations, for our range of  $b$ -values, bound the mass-loss rate in *neutral* hydrogen to  $\dot{M}_{HI} = 3.7 \times 10^5 - 2.3 \times 10^6 \text{ g s}^{-1}$ .

The mass-loss rate depends linearly on the  $b$ -value. So, if the  $b$ -value at the exobase, where the wind is launched, differs from  $b$ -values we have calculated, the mass-loss rate would differ correspondingly. Because the planet is so close to its host star, the EUV flux and charge exchange with the stellar wind will ionize most of the escaping hydrogen and only a small fraction will be neutral in the outer atmosphere. Koskinen et al. (2013) model the H and  $\text{H}^+$  density in the atmosphere of HD209458b as a function of planetary radius. In the upper atmosphere ( $R \sim 5R_p$ ) the neutral fraction is  $\sim 0.1$ . Assuming similar ionization conditions in the extended atmosphere of GJ436b, we correct for this neutral fraction, and calculate a total mass-loss rate

$$\dot{M} = 3.7 \times 10^6 - 2.3 \times 10^7 \text{ g s}^{-1}. \quad (12)$$

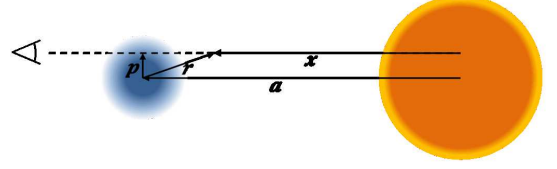


FIG. 5.— Geometry for mass-loss calculation. We consider a line of sight (LOS) toward the center of the star that passes through the planet's atmosphere at a distance  $p$  from the center of the planet, where  $x$  is measured along the LOS,  $\tau$  is measured from the center of the planet, and  $a$  is the distance between the star and planet.

Assuming the structure of GJ436b is similar to that of Neptune, and the atmosphere comprises 5-15% of the mass of the planet (Guillot 1999), and that the mass-loss rate is constant in time, this range of mass-loss rates give a range of atmospheric lifetimes of  $9.5 \times 10^{12} - 1.8 \times 10^{14}$  years, indicating that the atmosphere is stable over the lifetime of the star.

#### 4.2.2. EUV Heating to PdV Work

We also calculate the mass-loss rate following the analytical argument of Murray-Clay et al. (2009). We first calculate the amount of stellar EUV flux available to heat the atmosphere,

$$E_{heat} = \epsilon \pi F_{EUV} R_p^2 [\text{erg s}^{-1}]. \quad (13)$$

Here  $\epsilon$  is an efficiency factor,  $F_{EUV}$  (in  $\text{erg cm}^{-2} \text{ s}^{-1}$ ) is the stellar flux at the orbit of the planet from 300 – 912 Å (where the photoionization cross-section for hydrogen is largest; Murray-Clay et al. 2009), and  $R_p$  is the planetary radius ( $R_p = 0.38 R_{Jup}$ ). Using the model scaling relations of Linsky et al. (2014), we estimated the EUV flux based on the reconstructed Lyman- $\alpha$  luminosity (France et al. 2013). These calculated EUV luminosities are shown in Table 7. We then consider the PdV work required to liberate a unit mass from the gravitational well of the planet:

$$\frac{P \Delta V}{\rho R_p^2 H} \sim \frac{P R_p^3}{\rho R_p^2 H} \sim \frac{\rho g H R_p^3}{\rho R_p^2 H} \sim \frac{G M_p}{R_p}. \quad (14)$$

The mass-loss rate is then the ratio of the heat available to the work required to lift out mass:

$$\dot{M} = \frac{\epsilon \pi F_{EUV} R_p^2}{G M_p / R_p} = \frac{\epsilon \pi F_{EUV} R_p^3}{G M_p} = 1.1 \times 10^9 \text{ g s}^{-1}, \quad (15)$$

corresponding to a lifetime of  $4 \times 10^{11}$  years. Here we have assumed an efficiency  $\epsilon = 0.3$  and extrapolated an EUV flux  $F_{EUV} = 607 \text{ erg cm}^{-2} \text{ s}^{-1}$  from the reconstructed intrinsic Lyman- $\alpha$  flux. This argument is valid only if we are in the EUV driven, as opposed to X-ray driven, evaporation regime. According to Owen & Jackson (2012) for a Neptune mass planet with a density of  $1 \text{ g cm}^{-3}$  at a separation of 0.025 AU (for GJ436b: mass =  $1.35 M_{Nep}$ , density =  $1.69 \text{ g cm}^{-3}$ , separation = 0.029 AU) the critical X-ray luminosity at which the planetary wind will transition from X-ray driven to EUV driven is  $\sim 8 \times 10^{28} \text{ erg s}^{-1}$ . Kashyap et al. (2008) measure the the X-ray luminosity of GJ436 to be  $1.4 \times 10^{27} \text{ erg s}^{-1}$ , two orders of magnitude lower than the transition value, placing GJ436b well into the EUV driven evaporation regime.

TABLE 7  
EUV LUMINOSITY OF GJ436

Band	Luminosity [erg s <sup>-1</sup> ]
<100Å <sup>a</sup>	$1.45 \times 10^{27}$
100-200Å	$1.44 \times 10^{27}$
200-300Å	$1.26 \times 10^{27}$
300-400Å	$1.12 \times 10^{27}$
400-500Å	$2.48 \times 10^{25}$
500-600Å	$4.47 \times 10^{25}$
600-700Å	$5.82 \times 10^{25}$
700-800Å	$6.98 \times 10^{25}$
800-912Å	$9.41 \times 10^{25}$

<sup>a</sup> 5–124 Å luminosity from Kashyap et al. (2008).

These two methods give results that differ by 2 orders of magnitude. This is not surprising given that mass-loss calculations for HD209458 can vary by 4 orders of magnitude depending on method. Our range of mass-loss values are roughly consistent with the models of Ehrenreich et al. (2011). Their model transit curves can be seen in Figure 2. They predict a transit depth of 11% for a mass-loss rate of  $10^{10}$  g s<sup>-1</sup>. Their calculation of the mass-loss rate was based on the measured stellar X-ray (5 – 124 Å) luminosity,  $\log(L_X \text{ [erg s}^{-1}\text{]}) = 26.85^{+0.65}_{-0.89}$  (Hünsch et al. 1999). However, this X-ray luminosity arises in the stellar corona, and may not be representative of the majority of the longer wavelength EUV flux from GJ436, which is likely dominated by Lyman continuum emission from the transition region and upper chromosphere (Linsky et al. 2014). We find EUV luminosities lower than Ehrenreich et al. (2011), especially at wavelengths where the photoionization cross-section

for hydrogen is largest (300 – 900 Å; Murray-Clay et al. 2009). Their calculation also depends linearly on the heating efficiency ( $\eta$ , similar to  $\epsilon$  above) in the atmosphere, a parameter that is not well constrained. For  $\eta = 0.15$  they calculate  $\dot{M} = 1.60 \times 10^9$  g s<sup>-1</sup>, but this mass-loss rate can range between  $1.07 \times 10^8$  g s<sup>-1</sup> and  $1.07 \times 10^{10}$  g s<sup>-1</sup> for  $\eta$  between 0.01 and 1. Uncertainties in the neutral fraction that we use in our first calculation,  $\epsilon$  in our second calculation, and the parameters of the Ehrenreich et al. (2011) calculation leave a wide range for the possible mass-loss rate of GJ436b.

## 5. SUMMARY

We have analyzed new observations of GJ436. We used *HST*/STIS data to detect and characterize the extended atmosphere of GJ436b for the first time. We detected  $8.8 \pm 4.5\%$  absorption in the Lyman- $\alpha$  line at mid-transit, and used this transit depth to calculate a mass-loss rate in the range  $3.7 \times 10^6 - 1.1 \times 10^9$  g s<sup>-1</sup>, corresponding to an atmospheric lifetime of  $4 \times 10^{11} - 2 \times 10^{14}$  years. We also detected strong absorption after the optical transit with a depth of  $23.7 \pm 4.5\%$ . We confirmed that this extended egress is not a statistical fluctuation, and showed that it is unlikely to be due to stellar variability; the most likely explanation is that GJ436b is trailed by a comet-like tail of neutral hydrogen.

This material is based upon work supported by the National Science Foundation Graduate Research Fellowship Program under Grant No. DGE 1144083. The data presented here were obtained as part of *HST* Observing program #12034. KF acknowledges support through a NASA Nancy Grace Roman Fellowship during this work.

## REFERENCES

- Ben-Jaffel, L., & Ballester, G. E. 2013, *A&A*, 553, A52  
 Bourrier, V., & Lecavelier des Etangs, A. 2013, *A&A*, 557, A124  
 Budaj, J. 2013, *A&A*, 557, A72  
 Butler, R. P., Vogt, S. S., Marcy, G. W., et al. 2004, *ApJ*, 617, 580  
 Butler, R. P., Wright, J. T., Marcy, G. W., et al. 2006, *ApJ*, 646, 505  
 Charbonneau, D., Brown, T. M., Noyes, R. W., & Gilliland, R. L. 2002, *ApJ*, 568, 377  
 Deming, D., Harrington, J., Laughlin, G., et al. 2007, *ApJ*, 667, L199  
 Dere, K. P., Landi, E., Young, P. R., et al. 2009, *A&A*, 498, 915  
 Ehrenreich, D., & Désert, J.-M. 2011, *A&A*, 529, A136  
 Ehrenreich, D., Lecavelier Des Etangs, A., & Delfosse, X. 2011, *A&A*, 529, A80  
 Ekenbäck, A., Holmström, M., Wurz, P., et al. 2010, *ApJ*, 709, 670  
 France, K., Froning, C. S., Linsky, J. L., et al. 2013, *ApJ*, 763, 149  
 García Muñoz, A. 2007, *Planet. Space Sci.*, 55, 1426  
 Gillon, M., Pont, F., Demory, B.-O., et al. 2007, *A&A*, 472, L13  
 Guillot, T. 1999, *Science*, 286, 72  
 Guo, J. H. 2013, *ApJ*, 766, 102  
 Haswell, C. A., Fossati, L., Ayres, T., et al. 2012, *ApJ*, 760, 79  
 Henry, G. W., Marcy, G. W., Butler, R. P., & Vogt, S. S. 2000, *ApJ*, 529, L41  
 Holmström, M., Ekenbäck, A., Selsis, F., et al. 2008, *Nature*, 451, 970  
 Hu, R., & Seager, S. 2014, *ArXiv e-prints*, arXiv:1401.0948  
 Hünsch, M., Schmitt, J. H. M. M., Sterzik, M. F., & Voges, W. 1999, *A&AS*, 135, 319  
 Kashyap, V. L., Drake, J. J., & Saar, S. H. 2008, *ApJ*, 687, 1339  
 Knutson, H. A., Benneke, B., Deming, D., & Homeier, D. 2014, *Nature*, 505, 66  
 Koskinen, T. T., Harris, M. J., Yelle, R. V., & Lavvas, P. 2013, *Icarus*, 226, 1678  
 Koskinen, T. T., Yelle, R. V., Lavvas, P., & Lewis, N. K. 2010, *ApJ*, 723, 116  
 Lammer, H., Selsis, F., Ribas, I., et al. 2003, *ApJ*, 598, L121  
 Lecavelier des Etangs, A., Ehrenreich, D., Vidal-Madjar, A., et al. 2010, *A&A*, 514, A72  
 Lecavelier des Etangs, A., Bourrier, V., Wheatley, P. J., et al. 2012, *A&A*, 543, L4  
 Linsky, J. L., Fontenla, J., & France, K. 2014, *ApJ*, 780, 61  
 Linsky, J. L., Yang, H., France, K., et al. 2010, *ApJ*, 717, 1291  
 Linsky, J. L., Draine, B. T., Moos, H. W., et al. 2006, *ApJ*, 647, 1106  
 Loyd, R. O. P., & France, K. 2014, *The Astrophysical Journal Supplement Series*, 211, 9  
 Madhusudhan, N., & Seager, S. 2011, *ApJ*, 729, 41  
 Mayor, M., & Queloz, D. 1995, *Nature*, 378, 355  
 Murray-Clay, R. A., Chiang, E. I., & Murray, N. 2009, *ApJ*, 693, 23  
 Nidever, D. L., Marcy, G. W., Butler, R. P., Fischer, D. A., & Vogt, S. S. 2002, *ApJS*, 141, 503  
 Owen, J. E., & Jackson, A. P. 2012, *MNRAS*, 425, 2931  
 Pont, F., Gilliland, R. L., Knutson, H., Holman, M., & Charbonneau, D. 2009, *MNRAS*, 393, L6  
 Rappaport, S., Levine, A., Chiang, E., et al. 2012, *ApJ*, 752, 1  
 Schneider, J., Rauer, H., Lasota, J. P., Bonazzola, S., & Chassefiere, E. 1998, in *Astronomical Society of the Pacific Conference Series*, Vol. 134, *Brown Dwarfs and Extrasolar Planets*, ed. R. Rebolo, E. L. Martin, & M. R. Zapatero Osorio, 241  
 Seager, S., & Deming, D. 2010, *ARA&A*, 48, 631  
 Stevenson, K. B., Harrington, J., Nymeyer, S., et al. 2010, *Nature*, 464, 1161

- Swain, M. R., Vasisht, G., & Tinetti, G. 2008, *Nature*, 452, 329
- Swain, M. R., Tinetti, G., Vasisht, G., et al. 2009, *ApJ*, 704, 1616
- Tinetti, G., Vidal-Madjar, A., Liang, M.-C., et al. 2007, *Nature*, 448, 169
- Torres, G., Winn, J. N., & Holman, M. J. 2008, *ApJ*, 677, 1324
- Tremblin, P., & Chiang, E. 2013, *MNRAS*, 428, 2565
- van Leeuwen, F., ed. 2007, *Astrophysics and Space Science Library*, Vol. 350, Hipparcos, the New Reduction of the Raw Data
- Vidal-Madjar, A., Lecavelier des Etangs, A., Désert, J.-M., et al. 2003, *Nature*, 422, 143
- Vidal-Madjar, A., Désert, J.-M., Lecavelier des Etangs, A., et al. 2004, *ApJ*, 604, L69
- Yelle, R. V. 2004, *Icarus*, 170, 167
- . 2006, *Icarus*, 183, 508
- Zacharias, N., Finch, C. T., Girard, T. M., et al. 2012, *VizieR Online Data Catalog*, 1322, 0